



Vacancy Modulating $\text{Co}_3\text{Sn}_2\text{S}_2$ Topological Semimetal for Aqueous Zinc-Ion Batteries

Yuwei Zhao⁺, Yongbin Zhu⁺, Feng Jiang, Yiyao Li, You Meng, Ying Guo, Qing Li, Zhaodong Huang, Shaoce Zhang, Rong Zhang, Johnny C. Ho, Qianfan Zhang, Weishu Liu,^{*} and Chunyi Zhi^{*}

Abstract: Weyl semimetals (WSMs) with high electrical conductivity and suitable carrier density near the Fermi level are enticing candidates for aqueous Zn-ion batteries (AZIBs), meriting from topological surface states (TSSs). We propose a WSM $\text{Co}_3\text{Sn}_2\text{S}_2$ cathode for AZIBs showing a discharge plateau around 1.5 V. By introducing Sn vacancies, extra redox peaks from the $\text{Sn}^{4+}/\text{Sn}^{2+}$ transition appear, which leads to more Zn^{2+} transfer channels and active sites promoting charge-storage kinetics and Zn^{2+} storage capability. $\text{Co}_3\text{Sn}_{1.8}\text{S}_2$ achieves a specific energy of 305 Wh kg^{-1} (0.2 Ag^{-1}) and a specific power of 4900 W kg^{-1} (5 Ag^{-1}). $\text{Co}_3\text{Sn}_{1.8}\text{S}_2$ and $\text{Zn}_x\text{Co}_3\text{Sn}_{1.8}\text{S}_2$ benefit from better conductivity at lower temperatures; the quasi-solid $\text{Co}_3\text{Sn}_{1.8}\text{S}_2//\text{Zn}$ battery delivers 126 mAh g^{-1} (0.6 Ag^{-1}) at -30°C and a cycling stability over 3000 cycles (2 Ag^{-1}) with 85 % capacity retention at -10°C .

Introduction

Three-dimensional topological insulators (3DTIs) protected by time-reversal symmetry have strong metallic surface states covering the entire material.^[1] Topological surface states (TSSs) are derived from the bulk band inversions between the conduction and the valence band at the surface. Thus, they are robust against surface modifications and defects.^[2] They have a great influence on the surface electronic structure of the material, so the materials show

insulating in bulk but metallic at the surface. The topological phase materials with unique physical properties provide an ideal opportunity to understand the interaction between surface state, electron transfer, and surface electrochemical reaction, especially in a more realistic setting such as electrochemical batteries. Recently, topological behavior is further generalized to 3D bulk gapless systems, whose nondegenerate conduction and valence bands touch at points in 3D momentum space, named as the Weyl semimetals (WSMs).^[3] As the first magnetic WSM, $\text{Co}_3\text{Sn}_2\text{S}_2$ has attracted the most attention due to nontrivial TSSs, high conductivity and suitable carrier density around the Fermi level.^[4–7] TSSs of WSM $\text{Co}_3\text{Sn}_2\text{S}_2$ protected by bulk Weyl nodes are robust when exposure to environmental conditions like liquids. However, its peculiar properties are rarely explored in the electrochemical energy storage.

As cheap and sustainable energy economies flourish, electrochemical batteries including Li/Na/K⁻¹/Zn/Mg/Ca/Al-ion batteries offer promising solutions to store green energies.^[8] Up to now, metal oxides, organics and chalcogens are dominated electrode materials for all of these batteries. Taking the aqueous zinc-ion batteries (AZIBs) as an example, manganese-based materials,^[9,10] vanadium-based compounds,^[11,12] polyanion oxides,^[13,14] quinone compounds,^[15,16] and sulfur^[17–19] are typical cathodes. These materials are seriously hampered by their inherently limited electronic conductivity leading to a low charge-transfer rate and high electrode resistance. Therefore, it is important to enhance the conductivity of the electrode materials. Pre-intercalating the metal ions,^[20] coating or hybridizing conductive phases,^[21,22] and creating defects^[23,24] facilitate charge transfer. However, the efficient charge/ion transfer to all active sites remains a challenge, particularly when the size of electrode materials reaches a few microns. Thus, electrodes materials with inherently high conductivity are in great need.

Herein, WSM $\text{Co}_3\text{Sn}_{2-x}\text{S}_2$ ($x=0, 0.2$ and 0.4) are pioneered as cathodes of AZIB in a “water in salt” electrolyte. $\text{Co}_3\text{Sn}_2\text{S}_2//\text{Zn}$ battery exhibits a pair of redox located at 1.70/1.43 V. When Sn-vacancies are introduced, Sn^{2+} is activated and the $\text{Co}_3\text{Sn}_{1.8}\text{S}_2$ delivers an extra redox process ($\text{Sn}^{4+}/\text{Sn}^{2+}$). The number of active sites remarkably increases, which aids in a capacitance process. In situ X-ray diffraction (XRD), Raman, high resolution transmission electron microscopy (HRTEM), and ex situ X-ray photoelectron spectroscopy (XPS) tests confirm that Zn^{2+} is taking off/embedding in the interstitial Sn vacancies and the electrochemical transition occurs between Sn^{2+} and Sn^{4+} . Low-temperature electron

[*] Dr. Y. Zhao,^[†] Dr. Y. Meng, Dr. Y. Guo, Dr. Q. Li, Dr. Z. Huang, Dr. S. Zhang, Dr. R. Zhang, Prof. J. C. Ho, Prof. C. Zhi
 Department of Materials Science and Engineering
 City University of Hong Kong
 Hong Kong (China)
 E-mail: cy.zhi@cityu.edu.hk

Dr. Y. Zhu,^[†] Dr. F. Jiang, Prof. W. Liu
 Department of Materials Science and Engineering
 Southern University of Science and Technology
 Shenzhen (China)
 E-mail: liuws@sustech.edu.cn

Dr. Y. Li, Prof. Q. Zhang
 School of Materials Science and Engineering, Beihang University
 Beijing (China)
 Prof. C. Zhi
 Centre for Functional Photonics, City University of Hong Kong
 Kowloon, Hong Kong (China)

[†] These authors contributed equally to this work.

 Supporting information and the ORCID identification number(s) for the author(s) of this article can be found under:
 <https://doi.org/10.1002/anie.202111826>.

paramagnetic resonance (EPR) tests and positron lifetime spectra of $\text{Co}_3\text{Sn}_{2-x}\text{S}_2$ emphasize the Sn-vacancy concentration difference. Galvanostatic intermittent titration technique (GITT) shows that moderate introduction of Sn vacancies contributes to the improvement of Zn^{2+} diffusion rate. Benefitting from better conductivities of both $\text{Co}_3\text{Sn}_{1.8}\text{S}_2$ and $\text{Zn}_x\text{Co}_3\text{Sn}_{1.8}\text{S}_2$ at lower temperatures, $\text{Co}_3\text{Sn}_{1.8}\text{S}_2/\text{Zn}$ batteries deliver an excellent low-temperature rate capability and cycling stability.

Results and Discussion

The $\text{Co}_3\text{Sn}_{2-x}\text{S}_2$ ($x=0, 0.2$ and 0.4) ingots are synthesized via a conventional solid-state sintered method. The XRD patterns of $\text{Co}_3\text{Sn}_{2-x}\text{S}_2$ are shown in Figure 1a. All the reflections can be indexed to a P1 space group from trigonal crystal by reducing the symmetry corresponding to $\text{Co}_3\text{Sn}_2\text{S}_2$,

showing a high purity of the sample. $\text{Co}_3\text{Sn}_2\text{S}_2$ as a member of the Shandite family shows hexagonal Kagome lattices with Sn atoms in central locations assigned to the R-3 m(166) space group (Supporting Information, Figure S1a).^[25] Figure 1b and Figure S1b represents XRD patterns of $\text{Co}_3\text{Sn}_{1.8}\text{S}_2$ and $\text{Co}_3\text{Sn}_{1.6}\text{S}_2$ powders and their corresponding Rietveld refinement, respectively, showing that the ball-milling powders after sintering treatment are still the pure phase without any impurities introduced. The structure of the $\text{Co}_3\text{Sn}_{2-x}\text{S}_2$ system is clearly manifested in the form of [S-(Co_3Sn)-S]-Sn group arranged along the c axis (Figure 1c; Figure S1c–n) and the corresponding refined structural parameters are listed in Table S1 (Supporting Information).^[26] There are two kinds of Sn atoms marked as Sn1 (gray balls) and Sn2 (brown balls) which occupy different positions. For the $\text{Co}_3\text{Sn}_{1.8}\text{S}_2$ crystal structure, the Sn vacancy occupies Sn1 site first (Figure 1c). A similar phenomenon of highly occupied Sn1 sites and the minority occupied Sn2 sites is also observed in the $\text{Co}_3\text{Sn}_{1.6}\text{S}_2$

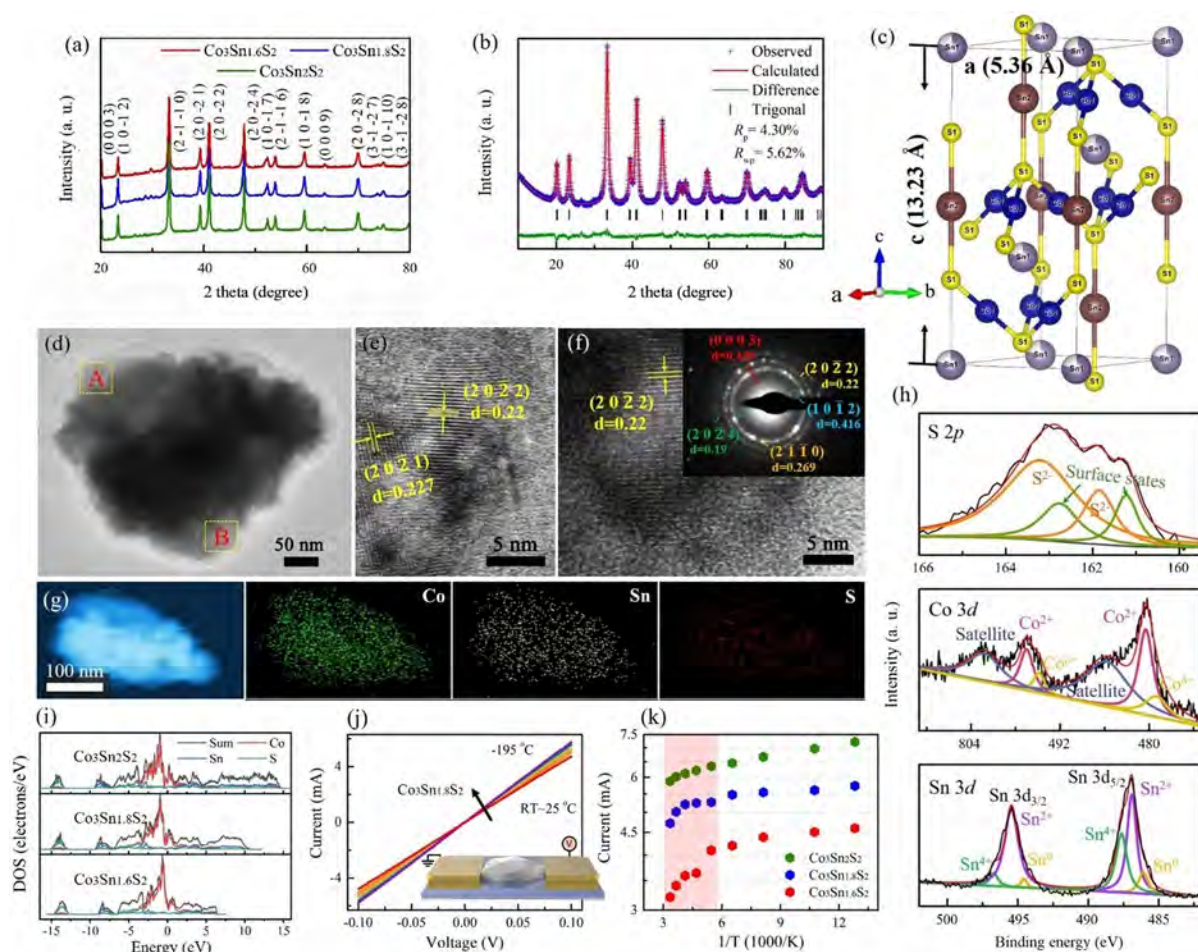


Figure 1. Structural analysis of prepared $\text{Co}_3\text{Sn}_{2-x}\text{S}_2$ ($x=0, 0.2$ and 0.4). a) XRD patterns of $\text{Co}_3\text{Sn}_{2-x}\text{S}_2$ crystal pellets. b) Rietveld refined XRD pattern of $\text{Co}_3\text{Sn}_{1.8}\text{S}_2$ powders and c) the corresponding crystal structure showing the Sn-deficient sites denoted as white spheres. d) HRTEM image of $\text{Co}_3\text{Sn}_{1.8}\text{S}_2$; Co (blue spheres), Sn (gray spheres), S (yellow spheres). e, f) The enlarged parts from the yellow boxes in (d). The inset SAED pattern shows high crystallinity of $\text{Co}_3\text{Sn}_{1.8}\text{S}_2$. g) Annular dark-field scanning transmission electron microscopy (ADF-STEM) image and corresponding EDS mappings of the $\text{Co}_3\text{Sn}_{1.8}\text{S}_2$ sample. h) High-resolution XPS spectra of S 2p, Co 3d and Sn 3d of $\text{Co}_3\text{Sn}_{1.8}\text{S}_2$. i) The partial density of states (PDOS) and total density of states (TDOS) patterns of $\text{Co}_3\text{Sn}_{1.6}\text{S}_2$, $\text{Co}_3\text{Sn}_{1.8}\text{S}_2$, and $\text{Co}_3\text{Sn}_2\text{S}_2$; Co (red line), Sn (blue line), S (green line), and total contributions (black lines). j) I-V curves as a function of temperature of $\text{Co}_3\text{Sn}_{1.8}\text{S}_2$ with an illustration of the $\text{Co}_3\text{Sn}_{1.8}\text{S}_2$ device assembled for electrical transport tests. k) The temperature-dependent current analysis on the $\text{Co}_3\text{Sn}_{2-x}\text{S}_2$ devices. The red region indicates the temperature range of 25–30°C.

crystal structure (Figure S1c–n). Comparing the lattice parameters of the three compositions, introducing Sn vacancy leads to the expansion of the lattice parameter *c* and the slight contraction of the lattice parameters of *a* and *b* (Table S1).

Figure S2 and S3, and Figure 1d and 1e are the scanning electron microscopy (SEM) and HRTEM images of the $\text{Co}_3\text{Sn}_{1.8}\text{S}_2$ showing irregular particles with particle sizes around hundreds of nanometers. HRTEM further reveals the high crystallinity of $\text{Co}_3\text{Sn}_{1.8}\text{S}_2$. Lattice-fringe spacings of 0.269 (Figure S3b), 0.227 and 0.220 nm are assigned to the (2 $\bar{1}\bar{1}$ 0), (20 $\bar{2}$ 1) and (20 $\bar{2}$ 2) planes of $\text{Co}_3\text{Sn}_{1.8}\text{S}_2$, respectively. Selected area electron diffraction (SAED) is conducted at location B in Figure 1d and shown in the inset of Figure 1f. The diffraction rings indicate the polycrystalline nature of $\text{Co}_3\text{Sn}_{1.8}\text{S}_2$ consistent with the XRD result. The elemental mapping (Figure 1g; Figure S2) confirms the uniform distribution of Co, Sn and S elements. XPS provides information of chemical composition and atomic valence states. As shown in Figure S4a–c and Figure 1h, there are three types of peaks for Sn 3d_{5/2} and Sn 3d_{3/2} spectra corresponding to Sn⁰ at 494.2 and 485.8 eV, Sn^{II} at 495.4 and 486.9 eV and Sn^{IV} states at 496.4 and 487.6 eV, respectively. Interestingly, with more Sn vacancy is introduced, the content of Sn²⁺ state increases from 45% ($\text{Co}_3\text{Sn}_2\text{S}_2$) to 87% ($\text{Co}_3\text{Sn}_{1.8}\text{S}_2$) and 80% ($\text{Co}_3\text{Sn}_{1.6}\text{S}_2$). The Sn vacancy greatly activates the Sn²⁺. S 2p core level spectra exhibit binding energies of 163.4 and 162.0 eV, corresponding to the S²⁻. Peaks at 163.0 and 161.5 eV are assigned to surface-derived contribution in $\text{Co}_3\text{Sn}_{2-x}\text{S}_2$.^[27] For Co 3d spectra, the peaks at 797.3 and 781.2 eV are from Co²⁺ and peaks at 794.6 and 779.2 eV are associated with Co^{δ+}, while the binding energies located at 803 and 785.3 eV are assigned to satellite structure for Co²⁺ and Co^{δ+} states. The above results indicate that the electron configuration of $\text{Co}_3\text{Sn}_{2-x}\text{S}_2$ is likely to be $(\text{Co}^{\delta+})_3(\text{Sn}^{2-\alpha})_{2-x}(\text{S}^{2-})_2$.^[26] Band structure calculation based on the first-principle calculation is applied on $\text{Co}_3\text{Sn}_x\text{S}_2$ (*x* = 2, 1.8 and 1.6) and the results are presented in Figure S5. Herein, $\text{Co}_3\text{Sn}_2\text{S}_2$ is confirmed to be semimetal where a considerable band gap appears in the band structure of spin-down electrons whereas the spin-up band is metallic (Figure S5a). Moreover, linear band crossing is observed near Fermi level in spin-up channels indicating its topological potential of Weyl-semimetal.^[6,28] Calculations on $\text{Co}_3\text{Sn}_{1.8}\text{S}_2$ (Figure S5b) and $\text{Co}_3\text{Sn}_{1.6}\text{S}_2$ (Figure S5c) reveal that the introduction of vacancies causes the electrons that should have formed bonds to be released. Meanwhile, the densities of states (DOS) calculations on $\text{Co}_3\text{Sn}_{2-x}\text{S}_2$ are also performed and the results are shown in Figure 1i exhibiting no significant variation is induced in electronic structure of $\text{Co}_3\text{Sn}_{2-x}\text{S}_2$ by Sn vacancies. Moreover, a slight rise of DOS could be observed at the energy a bit lower than the Fermi level, corresponding to the filled gap of spin-down channels in the band structure of $\text{Co}_3\text{Sn}_{2-x}\text{S}_2$. The relationship between electronic conductivities of $\text{Co}_3\text{Sn}_{2-x}\text{S}_2$ particles and temperature is studied by the direct-current electric transport test (Figure S6a–c; Figure 1j–k). The conductivity of the three samples increases with a decrease in temperature. Especially in the temperature range of 25–−30 °C shown in the red region of Figure 1k, the conductance increase of $\text{Co}_3\text{Sn}_{2-x}\text{S}_2$ particles is significant. As Sn vacancies are introduced, the

particle conductance (*G*) gets a little worse presented as $G(\text{Co}_3\text{Sn}_2\text{S}_2) > G(\text{Co}_3\text{Sn}_{1.8}\text{S}_2) > G(\text{Co}_3\text{Sn}_{1.6}\text{S}_2)$. The enhanced conductance at low temperatures is different from typical metal oxides.

Electrochemical properties of the $\text{Co}_3\text{Sn}_{2-x}\text{S}_2$ (*x* = 0, 0.2 and 0.4) samples are studied in coin cells. Figure 2a shows the cyclic voltammogram (CV) curves of Zn// $\text{Co}_3\text{Sn}_{2-x}\text{S}_2$ (*x* = 0, 0.2 and 0.4) batteries at 2 mV s^{−1} in 1 m Zn(TFSI)₂ and 21 m LiTFSI aqueous electrolyte. For $\text{Co}_3\text{Sn}_2\text{S}_2$, a pair of oxidation/reduction peak are observed at 1.70/1.43 V, corresponding to the insertion and extraction of Zn²⁺ (see the energy storage mechanism below for the detailed analysis). For $\text{Co}_3\text{Sn}_{1.8}\text{S}_2$, two pairs of oxidation/reduction peaks are shown at 1.64/1.5 and 1.25/1.08 V. The polarization voltage (0.14 V) of the $\text{Co}_3\text{Sn}_{1.8}\text{S}_2$ gets smaller compared to that (0.27 V) of the $\text{Co}_3\text{Sn}_2\text{S}_2$. The extra pair of peaks (1.25/1.08 V) is attributed to the valence change of Sn from Sn⁴⁺ and Sn²⁺ ($\text{Sn}^{4+} + \text{Zn} \leftrightarrow \text{Sn}^{2+} + \text{Zn}^{2+}$, *E* = 0.91 V). For $\text{Co}_3\text{Sn}_{1.6}\text{S}_2$, the redox peak is not significant, and the current associated with oxygen production increases revealing the instability of the $\text{Co}_3\text{Sn}_{1.6}\text{S}_2$ electrode. CVs of $\text{Co}_3\text{Sn}_{1.6}\text{S}_2$, $\text{Co}_3\text{Sn}_{1.8}\text{S}_2$ and $\text{Co}_3\text{Sn}_2\text{S}_2$ at different scan rates of 0.5–5 mV s^{−1} are displayed in Figure S7a,d,g. To explore the charge-storage kinetics, the linear fit of log(*i*) versus log(*v*) plot at redox peaks is carried out for $\text{Co}_3\text{Sn}_{1.6}\text{S}_2$, $\text{Co}_3\text{Sn}_{1.8}\text{S}_2$ and $\text{Co}_3\text{Sn}_2\text{S}_2$ (Figure S7b,e,h) according to the equation:^[29] $i = av^b$, namely current (*i*) dependence on the sweep rate (*v*). A value of *b* equals 0.5 demonstrates the current controlled by semi-infinite diffusion, and *b* equal to 1 manifests capacitive behavior.^[30] For $\text{Co}_3\text{Sn}_{1.8}\text{S}_2$, the calculated *b* values of the cathodic peaks are 0.86 and 0.85 revealing a largely diffusion-controlled battery behavior. Similarly, the $\text{Co}_3\text{Sn}_{1.6}\text{S}_2$ and $\text{Co}_3\text{Sn}_2\text{S}_2$ manifest a diffusion-dominated kinetic behavior with their *b* values of the cathodic peaks ranging from 0.67 to 0.72. Subsequently, the battery-type contribution can be distinguished from the capacitive contribution using a formula:^[31] $I = k_1v + k_2v^{1/2}$, *i* at any voltage (*V*) is a combination of capacitor-like (*k*₁*v*) and diffusion-controlled intercalation (*k*₂*v*^{1/2}) fractions. Figure S7c,f,i show that battery-type contribution to charge storage in $\text{Co}_3\text{Sn}_2\text{S}_2$, $\text{Co}_3\text{Sn}_{1.8}\text{S}_2$, and $\text{Co}_3\text{Sn}_{1.6}\text{S}_2$ accounts for 30%, 32% (Figure 2c) and 30% at 2 mV s^{−1}, respectively. With the introduction of Sn vacancies, the contribution of diffusion-controlled intercalation behavior increases at first due to the redox reaction of activated Sn for $\text{Co}_3\text{Sn}_{1.8}\text{S}_2$ (32%) and then descends due to the further enhanced Faradaic reactions to store charge in $\text{Co}_3\text{Sn}_{1.6}\text{S}_2$ (30%). Analogously, the capacitance and battery-type contributions at different rates are calculated and concluded in Figure 2d. At the scan rate of 0.5 mV s^{−1}, around 58% of the total current is capacitive-limited. As the scan rate increases, the contribution ratio of the capacitive process increases steadily. Since the number of active sites increases and the diffusion limiting process is much slower than the surface capacitive effect, the capacitive process shows a dominate role in the total capacity.

Worth mentioning is that it takes more than 200 cycles to activate $\text{Co}_3\text{Sn}_2\text{S}_2$ electrode (Figure S8a) and achieve the capacity of 160.7 at 1 Ag^{−1}. However, $\text{Co}_3\text{Sn}_{1.8}\text{S}_2$ and $\text{Co}_3\text{Sn}_{1.6}\text{S}_2$ just need 5 and 12 cycles to reach optimal capacities of 250.7 and 239.1 mAh g^{−1}, respectively (Figure 2b

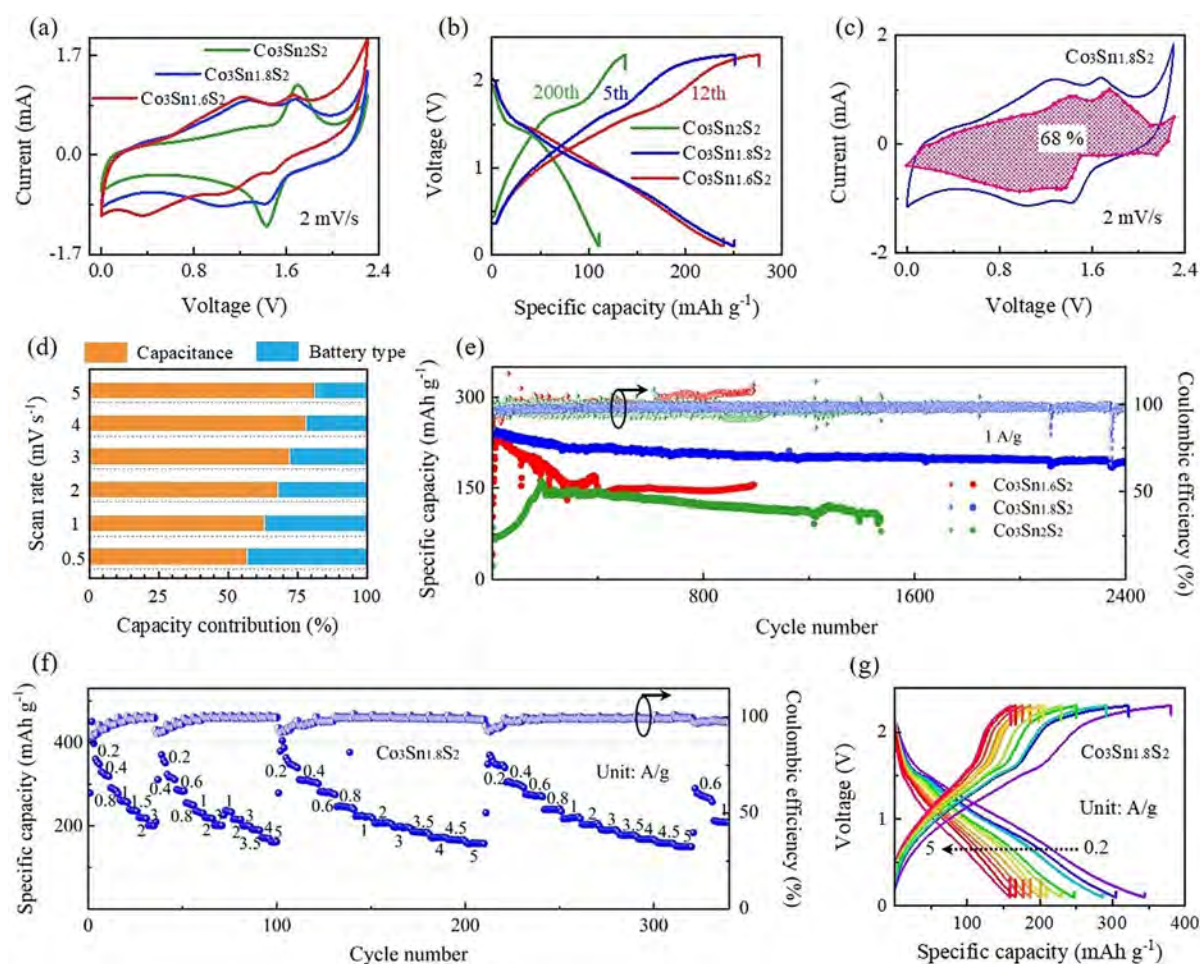


Figure 2. Electrochemical performance of Zn//Co₃Sn_{2-x}S₂ ($x=0, 0.2$ and 0.4) batteries using 1 m Zn(TFSI)₂ and 21 m LiTFSI aqueous electrolyte. a) CV curves of the Zn//Co₃Sn_{2-x}S₂ batteries at 2 mV s⁻¹. b) GCD curves of the fully activated Zn//Co₃Sn_{2-x}S₂ batteries at 1 A g⁻¹. c) The capacitance contribution to charge storage shown by the grid region. d) Capacitance and battery type contribution to capacity of the Zn//Co₃Sn_{1.8}S₂ batteries at different scan rates. e) Cycling performance and corresponding CE at 1 A g⁻¹. f) Rate capability with the current densities varying from 0.2 to 5 A g⁻¹ and g) corresponding GCD profiles.

and Figure S8b,c). Co₃Sn_{1.8}S₂ and Co₃Sn_{1.6}S₂ exhibit 1.56 and 1.49 times the electrochemical capacity of Co₃Sn₂S₂. The results can indirectly prove that the number of Zn²⁺ diffusion channels and electrochemical active sites increases after introducing the Sn vacancies. Co₃Sn₂S₂ displays a distinct discharge plateau at around 1.52 V, while no obvious discharge plateau for Co₃Sn_{1.6}S₂ are observed in accordance with the CV results. GCD profiles of Co₃Sn_{1.8}S₂ between 2nd and 1000th cycles are plotted in Figure S8b. Two discharge plateaus around 1.5 and 1.0 V are observed, corresponding to region I and region II, respectively. The battery delivers stable and low overpotentials, and limited capacity fade. Followed by cycle stability in Figure 2e, after 3000 cycles with a stable coulombic efficiency (CE) around 100%, the Zn//Co₃Sn_{1.8}S₂ battery still maintains a 83.3% discharge capacity retention of 195.7 mAh g⁻¹ at 1 A g⁻¹, which well rivals Zn//Co₃Sn₂S₂ battery (58.1%, 96 mAh g⁻¹, 1460 cycles) and Zn//Co₃Sn_{1.6}S₂ battery (65.7%, 156 mAh g⁻¹, 997 cycles). The CE of Co₃Sn_{1.6}S₂ drops sharply after 600 cycles ascribed to the structural collapse and poor connectivity proved by SEM images (Figure S9i-l). The number of Co₃Sn₂S₂ particles on

the surface decreased obviously after cycling (Figure S9a-d). In contrast, the number and connectivity of the Co₃Sn_{1.8}S₂ grains do not change too much as the cycle progresses, contributing to a stable cycle performance (Figure S9e-h).

Apparently, Co₃Sn₂S₂ goes through an activation stage about 100 cycles at various current densities, and then the capacities reaches the maximum of 199, 148.6, 120.4, 109.7, and 94.5 mAh g⁻¹ at 0.2, 0.8, 3, 4, and 5 A g⁻¹, respectively (Figure S10). Co₃Sn_{1.6}S₂ and Co₃Sn_{1.8}S₂ have much higher initial capacities than those of Co₃Sn₂S₂ (Figure 2f; Figure S10). After 100 cycles, the capacities of Co₃Sn_{1.6}S₂ fade to 246.4–113 mAh g⁻¹ at 0.2–5 A g⁻¹. Impressively, the reversible capacities of Co₃Sn_{1.8}S₂ almost returns to its initial capacities of 346, 308, 282, 248.2, 223.7, 208.7, 197.6, 186.3, 173, 167.3 and 158 mAh g⁻¹ when the current density is reverted to 0.2–5 A g⁻¹ after 100 cycles. The corresponding GCD profiles are shown in Figure S10 and Figure 2g. With the increase of current density, the linear characteristic of GCD profiles becomes more and more apparent. Taken together, both the cyclic stability and the rate capability of the Co₃Sn_{1.8}S₂ conspicuously outperform the other two materials attributed

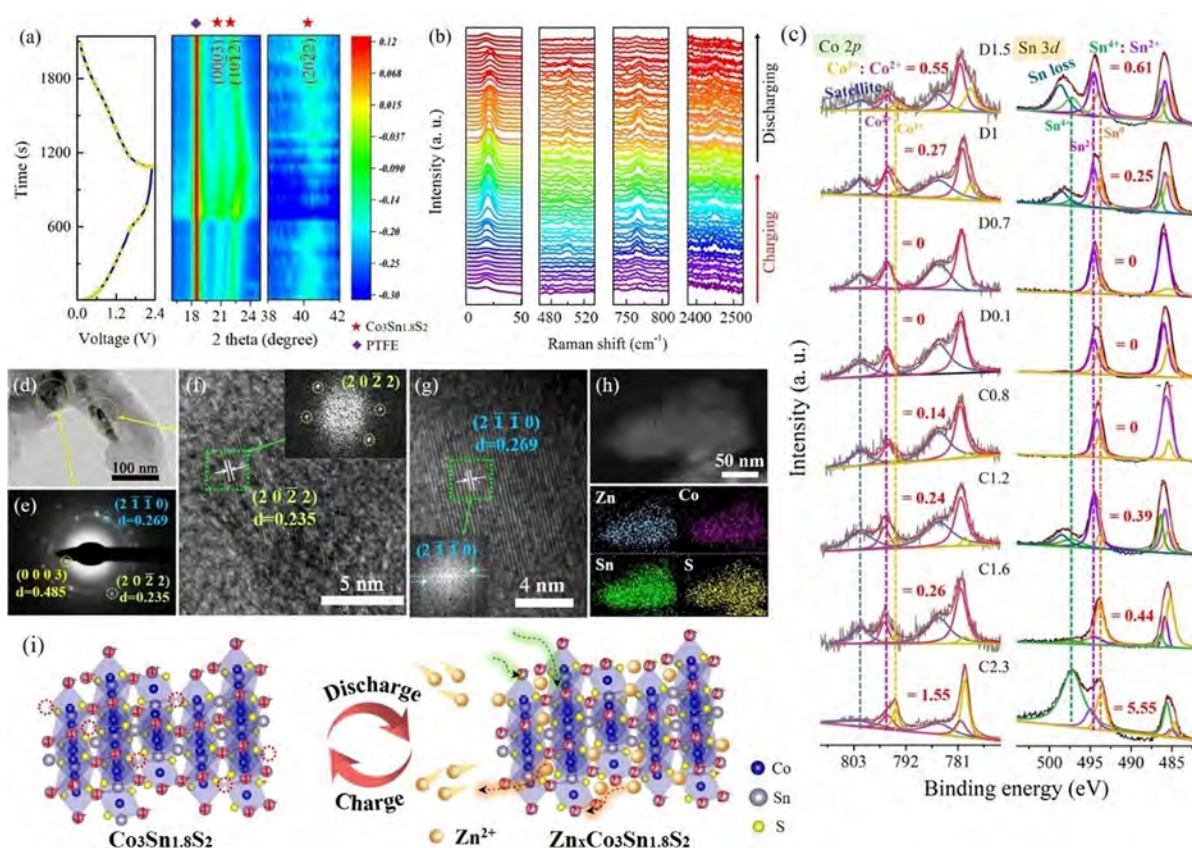


Figure 3. The structural evolution and charge-storage mechanism of the Co₃Sn_{1.8}S₂ electrode. a) Contour plot of in situ XRD measurements of Co₃Sn_{1.8}S₂ during the second charging and discharging with corresponding galvanostatic voltage-time curves at 0.3 A g⁻¹; crystalline planes of PTFE (purple diamonds) and Co₃Sn_{1.8}S₂ (red five-pointed stars). b) In situ Raman spectra of the Co₃Sn_{1.8}S₂ electrode corresponding to the second charging and discharging in (a). Red five-pointed stars represent the vibration modes of Co₃Sn_{1.8}S₂. c) Ex situ Co 3d and Sn 3d XPS spectra of the Co₃Sn_{1.8}S₂ electrode at different charge and discharge states. D1.5 and C0.8 are the abbreviation of “discharge to 1.5 V” and “charge to 0.8 V”, respectively. The ratios of Co³⁺:Co²⁺ and Sn⁴⁺:Sn²⁺ are calculated based on the peak areas. d–g) HRTEM images and the SAED pattern of Co₃Sn_{1.8}S₂ particles after full discharge. The insets in (f) and (g) display the corresponding FFT patterns for the discharge product. h) EDS elemental mappings for Zn, Co, Sn, and S in the selected area. i) Illustration of removal or embedding of Zn²⁺ from/in Co₃Sn_{1.8}S₂ during the charge/discharge process. The red dotted circles represent the Sn vacancies.

to the stable crystal structure,^[32,33] injected new electrochemical active sites,^[34] and high conductivity.^[35,36]

To further gain insights into the charge-storage mechanism, the structure evolution of Co₃Sn_{1.8}S₂ on charging and discharging is monitored via in situ XRD, in situ Raman, ex situ XPS and HRTEM. As shown in Figure 3a, in the charging process from 0.1 to 2.3 V, (0003), (10 $\bar{1}$ 2) and (20 $\bar{2}$ 2) characteristic peaks of the Co₃Sn_{1.8}S₂ cathode move toward higher angles, implying the deintercalation of Zn²⁺. Upon discharging to 0.1 V, these characteristic peaks shift back to the lower angles, suggesting the re-intercalation of Zn²⁺ and the formation of a Zn_xCo₃Sn_{1.8}S₂ compound. Subsequently, in situ Raman investigation of the Co₃Sn_{1.8}S₂ electrode in the charge/discharge process (0.1→2.3→0.1 V) is shown in Figure 3b. During charging, characteristic Raman peaks of the Co₃Sn_{1.8}S₂ electrode (Figure S11) appear gradually and grow stronger, indicating the Zn²⁺ deintercalation and enhanced crystallinity due to the formation of Co₃Sn_{1.8}S₂ crystal. Once discharging, these peaks become very faint and even disappear, demonstrating a structural evolution induced by the embedding of Zn²⁺. The XRD and Raman patterns after the

charge-discharge cycle nicely superimpose on the original Co₃Sn_{1.8}S₂ electrode, showing a completely reversible process. To elucidate the valence state variation of the Co₃Sn_{1.8}S₂ cathode under different charge and discharge conditions, ex situ XPS test is carried out (Figure 3c). For high-resolution Co 2p XPS spectra of the Co₃Sn_{1.8}S₂ cathode, during the course of discharging (2.3→0.1 V), the content of Co³⁺ located at 778.3 (2p_{3/2}) and 793.8 eV (2p_{1/2}) gradually decreases compared with that of Co²⁺ at 780.5 (2p_{3/2}) and 795.8 eV (2p_{1/2}). This process corresponds to the intercalation of Zn²⁺. Then, as the charging proceeds (0.1→2.3 V), the content proportion of Co³⁺ to Co²⁺ slowly increases from 0 to 1.55 owing to the extraction of Zn²⁺ from the Zn_xCo₃Sn_{1.8}S₂ structure. According to the previous XPS discussion, activated Sn²⁺ states act as the main peaks of high-resolution Sn 3d XPS spectra. Analogously, compared with Sn²⁺ signal peaks at 485.4 and 494.6 eV, peaks at 485.9 and 497.3 eV assigned to the Sn⁴⁺ signal become weaker and finally disappear upon discharging to 0.1 V (D1.5→D0.1). This evolution reveals that the insertion of Zn²⁺ induces the valence state transition from Sn⁴⁺ to Sn²⁺ in Co₃Sn_{1.8}S₂. During charging (C0.8→

C2.3), the content ratio of $\text{Sn}^{4+}:\text{Sn}^{2+}$ sharp increases from 0 to 5.55, manifesting a substantially increased Sn^{4+} proportion along with egress of Zn^{2+} . HRTEM images of the $\text{Co}_3\text{Sn}_{1.8}\text{S}_2$ cathode discharged to 0.1 V are also provided to verify the structural evolution (Figure 3 d). The corresponding SAED pattern (Figure 3 e) and HRTEM images (Figure 3 f,g) confirm the crystallinity of the $\text{Zn}_x\text{Co}_3\text{Sn}_{1.8}\text{S}_2$. The lattice spacings of (0003), (2 $\bar{1}$ 10) and (2022) planes are 0.485, 0.269 and 0.235 nm, respectively, demonstrating that the (0003) and (2022) lattice spacings of $\text{Zn}_x\text{Co}_3\text{Sn}_{1.8}\text{S}_2$ is about 10% and 7% larger than that of $\text{Co}_3\text{Sn}_{1.8}\text{S}_2$, which is consistent with the XRD measurements above. The above Zn^{2+} -intercalation/de-intercalation reaction mechanism is further confirmed by the EDS elemental mappings (Figure 3 h). When the $\text{Co}_3\text{Sn}_{1.8}\text{S}_2$ cathode is discharged to 0.1 V, Zn^{2+} uniformly distributes over the nanoparticle coincident with the distribution of Co, Sn and S. We further propose Zn^{2+} diffusion model of $\text{Co}_3\text{Sn}_{1.8}\text{S}_2$ (Figure 3 i). During the discharging process, Zn^{2+} migrates into octahedral sites of lattice and Sn vacancies, accompanied by the transition of Sn from tetravalent to bivalent. On charge, Zn^{2+} migrates back to the electrolyte entangled with the transition from Sn^{2+} to Sn^{4+} .

As the Sn vacancies show a remarkable role in Zn -ion storage, low-temperature EPR measurements of $\text{Co}_3\text{Sn}_{2-x}\text{S}_2$ are employed (Figure 4 a). The symmetrical resonance lines at $g=2.004$ and $g=1.894$ characteristic peaks are associated with the Co-S dangling bonds^[37] and Sn vacancies. The higher the intensity of the characteristic peak, the higher the concentration of vacancies. The signal intensity confirms that $\text{Co}_3\text{Sn}_{1.6}\text{S}_2$ has the highest Sn vacancy concentration, consistent with the initially designed composition. The types and relative concentrations of cation vacancies in the samples are investigated by positron lifetime spectra (Figure 4 b) and its derived lifetime parameters (Table 1). The $\text{Co}_3\text{Sn}_{2-x}\text{S}_2$ samples yield two lifetime components. The main short component (τ_1 , 154–166 ps) is attributed to the bulk lifetime, and the other component (τ_2 , 270–303 ps) could be credited to positron annihilation that trapped at Sn vacancies. It can be

Table 1: Positron lifetime parameters of $\text{Co}_3\text{Sn}_{2-x}\text{S}_2$ samples.

Sample	τ_1 [ps]	I_1 [%]	τ_2 [ps]	I_2 [%]	R-squared
$\text{Co}_3\text{Sn}_2\text{S}_2$	166	79.9	303	20.1	1.25
$\text{Co}_3\text{Sn}_{1.8}\text{S}_2$	166	65.5	296	34.5	1.19
$\text{Co}_3\text{Sn}_{1.6}\text{S}_2$	154	57.3	270	42.7	1.26

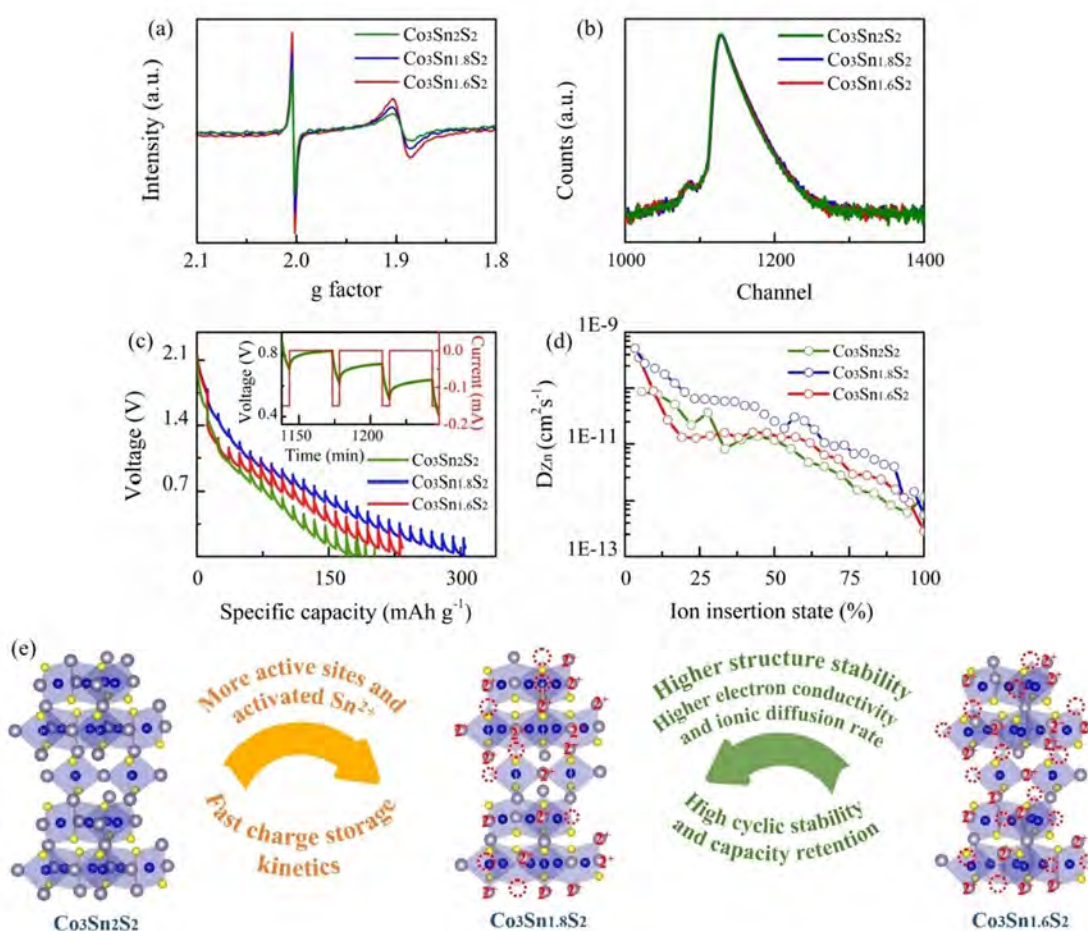


Figure 4. The effect of Sn vacancy on charge storage. a) Low-temperature EPR tests of $\text{Co}_3\text{Sn}_{2-x}\text{S}_2$ ($x=0, 0.2$ and 0.4). b) Positron lifetime spectra of $\text{Co}_3\text{Sn}_{2-x}\text{S}_2$. c) GITT profiles and d) corresponding calculated chemical diffusion coefficients for Zn^{2+} of $\text{Co}_3\text{Sn}_{2-x}\text{S}_2$. e) Advantages of $\text{Co}_3\text{Sn}_{1.8}\text{S}_2$ compared with $\text{Co}_3\text{Sn}_2\text{S}_2$ and $\text{Co}_3\text{Sn}_{1.6}\text{S}_2$; Co (blue ball), Sn (grey ball), S (yellow ball), Sn vacancy (dotted line circle).

clearly seen from the relative strength of positron lifetime (Table 1) that the content of Sn vacancies is the highest in $\text{Co}_3\text{Sn}_{1.6}\text{S}_2$, followed by $\text{Co}_3\text{Sn}_{1.8}\text{S}_2$. To verify the superiority of Sn vacancy on diffusion dynamics, the diffusion coefficients of Zn^{2+} in the $\text{Co}_3\text{Sn}_{2-x}\text{S}_2$ are calculated by the GITT (Figure 4c,d). The diffusion coefficient of the $\text{Co}_3\text{Sn}_{1.8}\text{S}_2$ is larger than those of $\text{Co}_3\text{Sn}_{1.6}\text{S}_2$ and $\text{Co}_3\text{Sn}_{2}\text{S}_2$ because less barrier for Zn^{2+} to migrate into octahedral sites and Sn vacancies. Hence, the benefits of $\text{Co}_3\text{Sn}_{1.8}\text{S}_2$ are demonstrated as follows (Figure 4e): (1) activate Sn^{2+} and provide more activated sites with impressive charge-storage capability and fast kinetic processes, (2) high structure stability with high electron conductivity and ionic diffusion rate achieving superior cycle stability and capacity retention.

Considering the unique electrical properties of WSM, we further test the electrochemical performance of $\text{Zn}/\text{Co}_3\text{Sn}_{1.8}\text{S}_2$ batteries in a wide temperature range using an antifreeze hydrogel electrolyte with high concentration of salts and ethylene glycol (HC-EGPAM). Figure 5a compares the rate capability of $\text{Zn}/\text{Co}_3\text{Sn}_{1.8}\text{S}_2$ from -30 – 50 °C: batteries show a higher capacity with a rise of temperature. At 50 °C, the battery delivers capacities of 363, 291, 257, 237, 219, 205, 194, 185, and 181 mAh g^{-1} at current densities of 0.6–

5 Ag^{-1} . When the temperature drops to -30 °C, the battery exhibits a discharge capacity of 71.5 mAh g^{-1} even at 5 Ag^{-1} and 126.4 mAh g^{-1} at 0.6 Ag^{-1} . Comparing to the room-temperature performance, the capacity retention remains around 45% at -30 °C. Compared with the capacities at low rate of 0.6 Ag^{-1} , capacity retention rates of 50% (50 °C), 57% (30 °C), 63% (10 °C), 60% (0 °C), 61% (-20 °C), and 56% (-30 °C) are achieved at a high rate of 5 Ag^{-1} (Figure 5b). The obtained impressive rate performance is closely related to the high conductivity of $\text{Co}_3\text{Sn}_{1.8}\text{S}_2$ at low temperatures.^[35]

Control batteries are assembled using common $\alpha\text{-MnO}_2$ and V_2O_5 as cathodes and the same antifreeze hydrogel electrolyte (Figure 5c). From -30 to 20 °C, $\text{Zn}/\text{Co}_3\text{Sn}_{1.8}\text{S}_2$ exhibits much superior low-temperature performance than $\text{Zn}/\alpha\text{-MnO}_2$, and $\text{Zn}/\text{V}_2\text{O}_5$ batteries. As the temperature decreases, the capacity of $\text{Zn}/\text{Co}_3\text{Sn}_{1.8}\text{S}_2$ decreases slowly compared to that of others. To further explain the excellent low-temperature performance, the temperature-dependent conductivity of the discharging product $\text{Zn}_x\text{Co}_3\text{Sn}_{1.8}\text{S}_2$ is assessed. The linear I - V relationship of the $\text{Zn}_x\text{Co}_3\text{Sn}_{1.8}\text{S}_2$ over the temperature range from -195 to 25 °C proves that the ohmic-like contacts (Figure 5d). The current versus $1000/T$ plots are displayed in the inset, indicating the conductivity

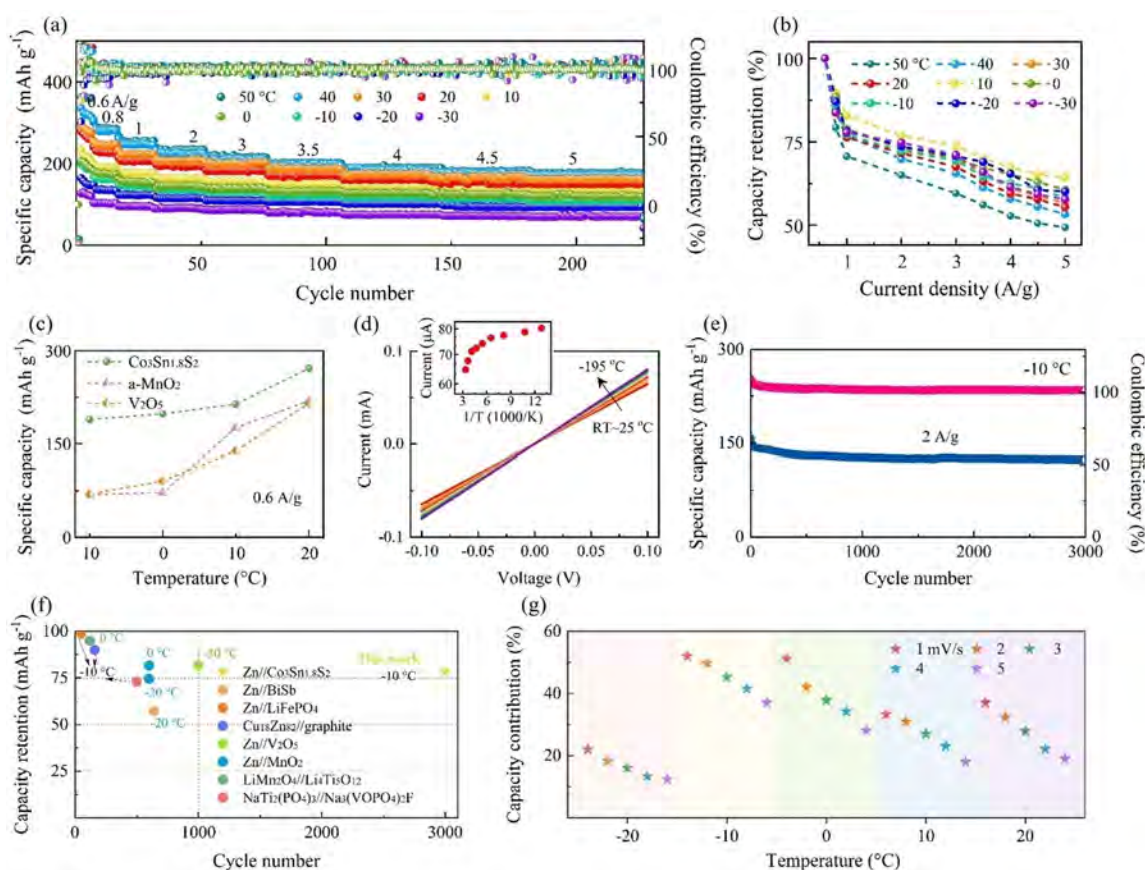


Figure 5. The low-temperature performance of $\text{Zn}/\text{Co}_3\text{Sn}_{1.8}\text{S}_2$ batteries. a) Rate capability of the $\text{Zn}/\text{Co}_3\text{Sn}_{1.8}\text{S}_2$ batteries from -30 to 50 °C. b) Comparison of capacity retention of $\text{Zn}/\text{Co}_3\text{Sn}_{1.8}\text{S}_2$ batteries at various temperatures. c) Temperature-dependent specific capacities of $\text{Co}_3\text{Sn}_{1.8}\text{S}_2$, $\alpha\text{-MnO}_2$ and V_2O_5 at 0.6 Ag^{-1} . d) I - V profiles at different temperatures of $\text{Zn}_x\text{Co}_3\text{Sn}_{1.8}\text{S}_2$ with the inset showing the temperature-dependent current analysis at 0.1 V . e) Long-cycle performance of the $\text{Zn}/\text{Co}_3\text{Sn}_{1.8}\text{S}_2$ battery at -10 °C. f) Comparison of the cycle stability of $\text{Zn}/\text{Co}_3\text{Sn}_{1.8}\text{S}_2$ batteries with other aqueous batteries at low temperatures. g) Temperature-dependent battery-type contribution to capacity of the $\text{Zn}/\text{Co}_3\text{Sn}_{1.8}\text{S}_2$ batteries at different scan rates.

of $\text{Zn}_x\text{Co}_3\text{Sn}_{1.8}\text{S}_2$ increases as the temperature goes down, similar with the behavior of $\text{Co}_3\text{Sn}_{1.8}\text{S}_2$. It should be noted that, although it exhibits expected metallic behavior, it is difficult to distinguish TSSs even if TSSs are still retained in $\text{Zn}_x\text{Co}_3\text{Sn}_{1.8}\text{S}_2$ by calculation. Furthermore, the $\text{Zn}/\text{Co}_3\text{Sn}_{1.8}\text{S}_2$ battery retains a stable capacity of 123.8 mAh g^{-1} even after 3000 cycles at -10°C and 2 Ag^{-1} (Figure 5e), delivering a highly competitive low-temperature stability compared to other reported aqueous batteries (Figure 5f).^[38–40] For common cathodes, the capacitance contribution to capacity is dominant at low temperatures. Notably, for the $\text{Co}_3\text{Sn}_{1.8}\text{S}_2$, when temperature drops from 20°C to -10°C , battery-type contribution to capacity increases from 37.06% to 52% at 1 mV s^{-1} as shown in Figure 5g. As lowering the temperature to -20°C , the battery-type capacity contribution drops dramatically to 22% (1 mV s^{-1}). Therefore, above -10°C , the battery-type contribution to capacity generally increases with decrease of the temperature.

The practicability of the $\text{Zn}/\text{Co}_3\text{Sn}_{1.8}\text{S}_2$ battery is demonstrated by the scalable pouch battery. Figure S12a shows the digital image of three $\text{Zn}/\text{Co}_3\text{Sn}_{1.8}\text{S}_2$ pouch batteries in series with an open-circuit voltage (OCV) of 5.32 V. Two pouch batteries in series light up orange and blue LEDs. Five pouch batteries in series (with an OCV of 11.06 V in Figure S12b) consisting of multilayer $\text{Co}_3\text{Sn}_{1.8}\text{S}_2$ cathodes and Zn anodes can power a “CITYU”-shape luminescence panel. Inset schematically shows the cell configuration with a cathode-separator-anode-separator-cathode-separator-anode stack. The corresponding Ragone plot of $\text{Co}_3\text{Sn}_{1.8}\text{S}_2$ compared to other representative AZIBs is demonstrated in Figure S12c, in which $\text{Co}_3\text{Sn}_{1.8}\text{S}_2$ shows superior specific power ($4903 \text{ W kg}^{-1}_{\text{Co}_3\text{Sn}_{1.8}\text{S}_2}$ at 5 Ag^{-1}) and specific energy ($305 \text{ Wh kg}^{-1}_{\text{Co}_3\text{Sn}_{1.8}\text{S}_2}$ at 0.2 Ag^{-1}).^[41–46]

Conclusion

We have presented a WSM $\text{Co}_3\text{Sn}_2\text{S}_2$ with excellent surficial electronic conductivity as the cathode of an AZIB. Systematic studies reveal that a moderate number of Sn vacancies is effective for activating Sn^{2+} and result in more Zn ion built-in channels and active sites, which promotes charge-storage kinetics (Zn^{2+} diffusion rate and electrical conductivity) and improves Zn-ion storage capability. The $\text{Co}_3\text{Sn}_{1.8}\text{S}_2$ cathode achieves a specific energy of $305 \text{ Wh kg}^{-1}_{\text{Co}_3\text{Sn}_{1.8}\text{S}_2}$ (capacity of 343.8 mAh g^{-1}) at 0.2 Ag^{-1} and a specific power greater than $4900 \text{ W kg}^{-1}_{\text{Co}_3\text{Sn}_{1.8}\text{S}_2}$ at 5 Ag^{-1} . The battery also retains a capacity of 193.8 mAh g^{-1} after 2970 cycles at 1 Ag^{-1} . Facilitated by better conductivity at lower temperatures of $\text{Co}_3\text{Sn}_{1.8}\text{S}_2$ and $\text{Zn}_x\text{Co}_3\text{Sn}_{1.8}\text{S}_2$, the quasi-solid $\text{Co}_3\text{Sn}_{1.8}\text{S}_2/\text{Zn}$ battery delivers a superior capacity of 126 mAh g^{-1} (0.6 Ag^{-1}) even at -30°C and an excellent cycling stability; that is, 85% of the initial capacity retention at -10°C and 2 Ag^{-1} after 3000 cycles. This work provides insights for designing electrodes by leveraging TSSs and incorporating vacancies to achieve synergistic benefits in battery performance.

Acknowledgements

The work is sponsored by GRFs under Project CityU 11212920, the Guangdong Innovative and Entrepreneurial Research Team Program (the Grant No. 2016ZT06G587), and the Shenzhen Sci-Tech Fund No. KYTDPT20181011104007.

Conflict of Interest

The authors declare no conflict of interest.

Keywords: aqueous zinc-ion batteries · tin vacancies · topological semimetals · Weyl semimetals

- [1] H. Chen, W. Zhu, D. Xiao, Z. Zhang, *Phys. Rev. Lett.* **2011**, *107*, 056804.
- [2] L. Muechler, H. Zhang, S. Chadov, B. Yan, *Angew. Chem. Int. Ed.* **2012**, *51*, 7221–7225; *Angew. Chem.* **2012**, *124*, 7333–7337.
- [3] J. Liu, D. Vanderbilt, *Phys. Rev. B* **2014**, *90*, 155316.
- [4] A. A. Burkov, M. D. Hook, L. Balents, *Phys. Rev. B* **2011**, *84*, 235126.
- [5] Y. Xing, J. Shen, H. Chen, L. Huang, Y. Gao, Q. Zheng, Y. Zhang, G. Li, B. Hu, G. Qian, L. Cao, X. Zhang, P. Fan, R. Ma, Q. Wang, Q. Yin, H. Lei, W. Ji, S. Du, H. Yang, W. Wang, C. Shen, X. Lin, E. Liu, B. Shen, Z. Wang, H. Gao, *Nat. Commun.* **2020**, *11*, 5613.
- [6] E. Liu, Y. Sun, N. Kumar, L. Muechler, A. Sun, L. Jiao, S. Yang, D. Liu, A. Liang, Q. Xu, J. Kroder, V. Süß, H. Borrmann, C. Shekhar, Z. Wang, C. Xi, W. Wang, W. Schnelle, S. Wirth, Y. Chen, S. T. B. Goennenwein, C. Felser, *Nat. Phys.* **2018**, *14*, 1125–1131.
- [7] Q. Wang, Y. Xu, R. Lou, Z. Liu, M. Li, Y. Huang, D. Shen, H. Wang, S. Wang, H. Lei, *Nat. Commun.* **2018**, *9*, 3681.
- [8] M. Armand, J. M. Tarascon, *Nature* **2008**, *451*, 652–657.
- [9] H. Li, C. Han, Y. Huang, Y. Huang, M. Zhu, Z. Pei, Q. Xue, Z. Wang, Z. Liu, Z. Tang, Y. Wang, F. Kang, B. Li, C. Zhi, *Energy Environ. Sci.* **2018**, *11*, 941–951.
- [10] N. Zhang, F. Cheng, J. Liu, L. Wang, X. Long, X. Liu, F. Li, J. Chen, *Nat. Commun.* **2017**, *8*, 405.
- [11] F. Wan, L. Zhang, X. Dai, X. Wang, Z. Niu, J. Chen, *Nat. Commun.* **2018**, *9*, 1656.
- [12] C. Liu, Z. Neale, J. Zheng, X. Jia, J. Huang, M. Yan, M. Tian, M. Wang, J. Yang, G. Cao, *Energy Environ. Sci.* **2019**, *12*, 2273–2285.
- [13] G. Li, Z. Yang, Y. Jiang, C. Jin, W. Huang, X. Ding, Y. Huang, *Nano Energy* **2016**, *25*, 211–217.
- [14] W. Li, K. Wang, S. Cheng, K. Jiang, *Energy Storage Mater.* **2018**, *15*, 14–21.
- [15] C. Han, J. Zhu, C. Zhi, H. Li, *J. Mater. Chem. A* **2020**, *8*, 15479–15512.
- [16] Y. Lu, Q. Zhang, L. Li, Z. Niu, J. Chen, *Chem* **2018**, *4*, 2786–2813.
- [17] W. Li, K. Wang, K. Jiang, *Adv. Sci.* **2020**, *8*, 3785–3794.
- [18] X. Wu, A. Markir, L. Ma, Y. Xu, H. Jiang, D. P. Leonard, W. Shin, T. Wu, J. Lu, X. Ji, *Angew. Chem. Int. Ed.* **2019**, *58*, 12640–12645; *Angew. Chem.* **2019**, *131*, 12770–12775.
- [19] Y. Zhao, D. Wang, X. Li, Q. Yang, Y. Guo, F. Mo, Q. Li, C. Peng, H. Li, C. Zhi, *Adv. Mater.* **2020**, *32*, e2003070.
- [20] Y. Yang, Y. Tang, S. Liang, Z. Wu, G. Fang, X. Cao, C. Wang, T. Lin, A. Pan, J. Zhou, *Nano Energy* **2019**, *61*, 617–625.

- [21] Y. Fu, Q. Wei, G. Zhang, X. Wang, J. Zhang, Y. Hu, D. Wang, L. Zuin, T. Zhou, Y. Wu, S. Sun, *Adv. Energy Mater.* **2018**, *8*, 1801445.
- [22] B. Wu, G. Zhang, M. Yan, T. Xiong, P. He, L. He, X. Xu, L. Mai, *Small* **2018**, *14*, e1703850.
- [23] Y. Xu, M. Zhou, X. Wang, C. Wang, L. Liang, F. Grote, M. Wu, Y. Mi, Y. Lei, *Angew. Chem. Int. Ed.* **2015**, *54*, 8768–8771; *Angew. Chem.* **2015**, *127*, 8892–8895.
- [24] W. Zou, J. Dong, Y. Luo, Q. Zhao, T. Xie, *Adv. Mater.* **2017**, *29*, 1606100.
- [25] M. A. Kassem, Y. Tabata, T. Waki, H. Nakamura, *Phys. Rev. B* **2017**, *96*, 014429.
- [26] G. Li, Q. Xu, W. Shi, C. Fu, L. Jiao, M. E. Kamminga, M. Q. Yu, H. Tueysuez, N. Kumar, V. Suess, R. Saha, A. K. Srivastava, S. Wirth, G. Auffermann, J. Gooth, S. Parkin, Y. Sun, E. K. Liu, C. Felser, *Sci. Adv.* **2019**, *5*, eaaw9867.
- [27] M. Holder, Y. S. Dedkov, A. Kade, H. Rosner, W. Schnelle, A. Leithe-Jasper, R. Wehrich, S. L. Molodtsov, *Phys. Rev. B* **2009**, *79*, 205116.
- [28] Z. Huang, T. Wang, H. Song, X. Li, G. Liang, D. Wang, *Angew. Chem. Int. Ed.* **2021**, *60*, 1011–1021; *Angew. Chem.* **2021**, *133*, 1024–1034.
- [29] H. S. Kim, J. B. Cook, H. Lin, J. S. Ko, S. H. Tolbert, B. Dunn, *Nat. Mater.* **2017**, *16*, 454–460.
- [30] J. Wang, J. Polleux, J. Lim, B. Dunn, *J. Phys. Chem. C* **2007**, *111*, 14925–14931.
- [31] A. J. Bard, L. R. Faulkner, *Electrochemical Methods: Fundamentals and Applications*, 2nd Ed., Wiley, **2001**.
- [32] Y. Zhao, L. Ma, Y. Zhu, P. Qin, H. Li, F. Mo, D. Wang, G. Liang, Q. Yang, W. Liu, C. Y. Zhi, *ACS Nano* **2019**, *13*, 7270–7280.
- [33] Q. Li, Y. Wang, F. Mo, D. Wang, G. Liang, Y. W. Zhao, Q. Yang, Z. D. Huang, C. Y. Zhi, *Adv. Energy Mater.* **2021**, *11*, 2003931.
- [34] Z. Li, Y. Ren, L. Mo, C. Liu, K. Hsu, Y. Ding, X. Zhang, X. Li, L. Hu, D. Ji, G. Cao, *ACS Nano* **2020**, *14*, 5581–5589.
- [35] Z. Jian, W. Luo, X. Ji, *J. Am. Chem. Soc.* **2015**, *137*, 11566–11569.
- [36] X. Li, N. Li, Z. Huang, Z. Chen, G. Liang, Q. Yang, M. Li, Y. Zhao, L. Ma, B. Dong, Q. F. Huang, J. Fan, C. Y. Zhi, *Adv. Mater.* **2021**, *33*, e2006897.
- [37] W. Zhong, Z. Wang, N. Gao, L. Huang, Z. Lin, Y. Liu, F. Meng, J. Deng, S. Jin, Q. Zhang, L. Gu, *Angew. Chem. Int. Ed.* **2020**, *59*, 22743–22748; *Angew. Chem.* **2020**, *132*, 22931–22936.
- [38] Q. Zhang, K. Xia, Y. Ma, Y. Lu, L. Li, J. Liang, S. Chou, J. Chen, *ACS Energy Lett.* **2021**, *6*, 2704–2712.
- [39] D. Reber, R. Kühnel, C. Battaglia, *ACS Mater. Lett.* **2019**, *1*, 44–51.
- [40] N. Yesibolati, N. Umirov, A. Koishybay, M. Omarova, I. Kurmanbayeva, Y. Zhang, Y. Zhao, Z. Bakenov, *Electrochim. Acta* **2015**, *152*, 505–511.
- [41] M. H. Alfaruqi, J. Gim, S. Kim, J. P. Duong, J. Jo, Z. Xiu, V. Mathew, J. Kim, *Electrochem. Commun.* **2015**, *60*, 121–125.
- [42] R. Trócoli, F. La Mantia, *ChemSusChem* **2015**, *8*, 481–485.
- [43] L. Zhang, L. Chen, X. Zhou, Z. Liu, *Sci. Rep.* **2015**, *5*, 18263.
- [44] S. Yang, C. Li, Y. Wang, S. Chen, M. Cui, X. Bai, *Energy Storage Mater.* **2020**, *33*, 230–238.
- [45] F. Mo, Y. Huang, Q. Li, Z. Wang, R. Jiang, W. Gai, C. Zhi, *Adv. Funct. Mater.* **2021**, *31*, 2010830.
- [46] Y. Zhao, Z. Chen, F. Mo, D. Wang, Y. Guo, Z. Liu, X. Li, Q. Li, G. Liang, C. Zhi, *Adv. Sci.* **2020**, *8*, 2002590.

Manuscript received: August 31, 2021

Revised manuscript received: October 1, 2021

Accepted manuscript online: October 15, 2021

Version of record online: November 25, 2021